Enhanced Coagulation Due to Evaporation and Its Effect on Nanoparticle Evolution

M. Z. JACOBSON,*,[†]
D. B. KITTELSON,[‡] AND W. F. WATTS[‡]

*Department of Civil and Environmental Engineering,
Stanford University, Stanford, California 94305-4020, and
Department of Mechanical Engineering, University of
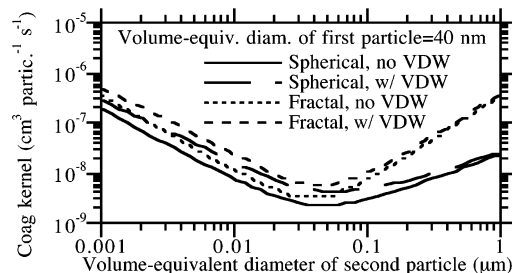Minnesota, Minneapolis, Minnesota 55455*

FIGURE 1. Calculated Brownian coagulation rate using equations from ref *17* when the volume-equivalent diameter of the first particle is 40 nm and that of the second varies from 1 to 1000 nm. The four curves shown in each figure account for when particles are spherical ($D_f = 3$) or fractal ($D_f = 1.7$ above 27 nm and $= 3$ below) and when van der Waals and viscous forces (VDW) were or were not included. Also, $A/k_BT = 200$, $T = 298.15$ K, and $p = 1$ atm.

A new explanation for the evolution of particles near a roadway is proposed. The explanation starts with data that suggest that small (<15 nm) liquid nanoparticles shed semivolatile organics (<C_{24}) almost immediately upon emission. It is shown here that the shrinking of these particles enhances their rates of coagulation by over an order of magnitude, and this appears important in helping to explain particle evolution further downwind, as measured by two datasets, including one reported here, and as found with a three-dimensional numerical model used to simulate the data. Enhanced coagulation in isolated emission puffs may also affect evolution. Neither condensation, complete evaporation, coagulation alone, nor preferential small-particle dilution appears to explain the evolution.

Introduction

Aerosol particles are the most unhealthful components of air pollution, and their health effects depend on their size and composition. Particle size and composition similarly affect visibility, clouds, weather, and climate. Most new particles by number are emitted, and vehicles are an important emission source. Measurements have indicated that emitted nanoparticle (<50 nm diameter) size distributions change rapidly with distance from a roadway source (*1–4*).

The greatest roadway emitters of particles per vehicle are diesel powered. The emitted small nanoparticles in diesel exhaust are generally semivolatile, containing primarily unburned fuel (C_{15}–C_{23} organics), unburned lubricating oil (C_{15}–C_{36} organics), and sulfate, and form during dilution and cooling of exhaust (e.g., *5–7*). Diesel vehicles also emit accumulation-mode particles (30–1000-nm diameter), which consist primarily of aggregates of tens to hundreds of graphite spherules with diameters ranging from about 5–50 nm with a mean of 25–35 nm that form during combustion (*5, 8–10*). Gasoline vehicles emit primarily semivolatile compounds with at least one peak of 20–30-nm diameter (*11*) and a larger peak smaller than 10 nm (*12*).

Several modeling studies have tried to explain particle evolution near a roadway (*2, 14–19*). In Jacobson and Seinfeld (*17*), enhanced Brownian coagulation due to van der Waals forces and fractal geometry was found to account for a greater

share of particle evolution than Brownian coagulation alone. However, coagulation alone was too slow to account fully for the rapid evolution. Subsequently, Zhang et al. (*19*) used "best fit" parameters in a 0-D model to try to explain particle evolution in terms of condensation/evaporation and dilution alone, ignoring coagulation. However, the size distributions fitted to obtain the conclusion were measured with a long-column scanning mobility particle sizer (SMPS) instrument, which misses about 75% of particle number due to diffusional losses below 20 nm (*20*). The conclusion also required the presence of a low-volatility-low-molar volume (LVLMV) C_1–C_3 emitted organic gas to overcome the Kelvin effect, allowing small particles to grow. However, the most relevant LVLMV are oxalic acid and malonic acid, yet only trace quantities of total organic acids (∼0.5%, *7* (p 1205)) or alkanedioc acids (*6* (p 2238)) have been found in diesel nanoparticles. Thus, another explanation is needed.

Here, one is offered. The explanation starts with data (*7*) that show that semivolatile (<C_{24}) organics evaporate almost immediately from liquid nanoparticles that form near the tailpipe by nucleation and condensation during initial dilution and cooling, and these particles contain unburned fuel (C_{15}–C_{23}), unburned lubricating oil (C_{15}–C_{36}), and sulfate (*5, 7, 21*). The evaporation rate depends significantly on temperature and carbon number (*7* (Figure 5)).

Second, as particles shrink, their coagulation rates with larger particles increase. This fact is demonstrated with Figure 1, which shows the coagulation rate of a 40-nm-diameter particle with a second particle of variable size. If the second particle is <40 nm and shrinks, its coagulation rate increases by up to 2 orders of magnitude. For pure Brownian motion in the free-molecular regime (e.g., *22* (eq 16.26)) the rate increases with decreasing size because a particle's thermal speed increases superlinearly with decreasing size. Although the total collision cross section of two particles decreases when one particle shrinks, the decrease is much smaller than the relative increase in thermal speed. In the transition regime, Brownian coagulation also increases with smaller size because diffusion increases with smaller size in the Cunningham slip-flow correction factor and in the Stokes–Einstein equation (*22* (eq 16.24)). Figure 1 here shows that van der Waals forces and collision with fractals (>27 nm in the figure) also enhance Brownian coagulation as particles shrink.

Methods

In sum, measurements suggest semivolatile components, which arise from nucleation and condensation during initial

* Corresponding author phone: 650-723-6836; fax: 650-725-9720; e-mail: jacobson@stanford.edu.
[†] Stanford University.
[‡] University of Minnesota.

dilution and cooling of exhaust, evaporate from nanoparticles following the initial condensation. As the particles move downwind and shrink further, their enhanced coagulation rates gradually reduce their concentrations relative to larger particles. This theory appears to explain observed downwind data (2–4), and is demonstrated next with a 3-D model, GATOR-GCMOM (17, 23, 24) applied to data from Los Angeles (3, 4) and Minnesota (presented here).

The model was first situated in West Los Angeles near Interstate 405 and Wilshire Boulevard. A single high-resolution limited-area grid of 100 W–E grid cells × 60 S–N grid cells × 22 layers at a resolution of 15 m × 15 m in the horizontal and 5 m in the vertical was used. Simulations for Los Angeles were run for a few minutes in the summer, so clouds and nesting from the large scale were neglected. Initialization and other aspects of the simulations were the same as in ref 17, except as described herein.

Whereas 10 aerosol size distributions, each with 17 discrete size bins, were treated in ref 17, only one distribution, but with 25 bins from 0.8 to 2000 nm diameter, 35 components per bin, including background and emitted particles, was treated here. Emitted particles dominated number concentration by 2 orders of magnitude relative to background particles, rendering the use of 1 versus 10 distributions of minor consequence over a short period.

The model treated number concentration of each size bin and mole concentration of individual components in each bin as prognostic variables. Number and mole concentrations were affected by emission, homogeneous nucleation, aerosol–aerosol coagulation, transport, dry deposition, and sedimentation. In addition, mole concentrations were affected by condensation, evaporation, hydration, dissolution, dissociation, and crystallization. Meteorology for gas and particle transport was calculated on-line, with feedback from the gases and particles through radiative transfer. The operator-split time step for model dynamics was 0.02 s, that of gas and particle transport was 0.4 s, and that of all physical and chemical processes (including emission, condensation, coagulation, etc.) was 1 s. Thus, all processes fed back to each other relatively rapidly.

Aerosol components treated within each size bin included individual C_{15}–C_{36} organic surrogates, a surrogate LVLMV species (oxalic acid), "other" organics, black carbon (BC), H_2O, $H_2SO_4(aq)$, HSO_4^-, SO_4^{2-}, H^+, NH_4^+, Na^+, NO_3^-, Cl^-, $NH_4NO_3(s)$, and soildust. Of the species, only BC, C_{15}–C_{36} organic surrogates, the LVLMV surrogate, and the sulfur species were emitted. The rest were present in background particles and, in the case of semivolatile inorganics, condensed or dissolved from the gas phase.

The C_{15}–C_{36} surrogates were alkanes, identified to be important in urban air (25) and in diesel exhaust (21, 7). The vapor pressures of these surrogates are similar to those of alkenes and several other organics of the same carbon numbers (26). Although soot contains many unresolved organics (21) with vapor pressures possibly different from those of alkanes, using alkane vapor pressures for unresolved mass should not alter conceptual findings here.

Because the dimensions of model grid cells were 15 m × 15 m × 5 m, the model did not resolve the tailpipes of vehicles. Instead, all condensation in the initial exhaust arising from its dilution and cooling to ambient temperature was assumed to be reflected in the emission size distribution. This assumption is justified for the model grid spacing used by the approximate equation for the temperature (K) of an exhaust plume, $T_p = [T_e + T_a(1 - D)]/D$, where T_e is the exhaust temperature (K), T_a is the ambient temperature, and D is the dilution ratio. Dilution ratios 2–3 m from a moving vehicle were measured in at least one study to be 600–4400 (27), suggesting that the exhaust plume temperature at this distance is close to the ambient temperature. Since 2–3 m
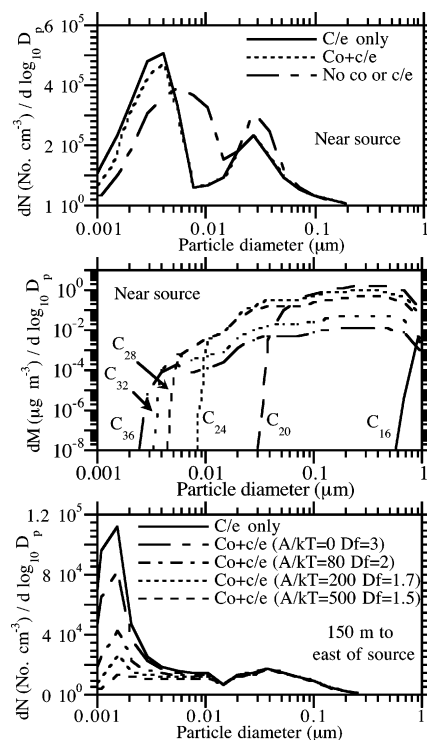

FIGURE 2. Base-case comparison of near-surface particle number distribution when condensation/evaporation alone ("C/e only") and coagulation+condensation/evaporation ("Co+c/e") were treated at (a) a grid cell along the line source of emission, and (c) 150 m to the east of source at the end of 3-D simulations. Panel a also shows results when no coagulation or condensation (No co or c/e) was treated. Panel b shows the distribution of C_{16}, C_{20}, C_{24}, C_{28}, C_{32}, and C_{36} organics in the particles shown in the "Co+c/e" curve in a. Panel c also shows results when different values of the Hamaker constant and fractal dimension were used. The base case was $A/k_BT = 200$ and $D_f = 1.7$ (above 27 nm but = 3 below), which were also the values used in a and b. Brownian coagulation alone is the $A/k_BT = 0$ and $D_f = 3$ curve. Dry deposition, transport, and turbulence were treated in all cases.

is smaller than the model grid spacing, emissions into a model grid cell were assumed to be at ambient temperature.

In sum, tailpipe emissions in the model were emitted into a model grid cell at the ambient temperature, and the emitted particle size distribution was assumed to contain all material that had condensed due to cooling from the exhaust temperature to the ambient temperature. Ambient temperatures in the model varied among grid cells over time due to diabatic energy transfer (e.g., latent heat exchange, radiative heating/cooling), adiabatic expansion/compression, and energy advection, but such temperature variations were small during these short simulations.

Particle constituents were emitted into a model grid cell assuming a size distribution whose overall shape down to 6 nm diameter was obtained from a fit to a composite average of data gathered 30 m from the Interstate 94 freeway in Minnesota as part of this study (please see "Discussion" for further information about the measurements). The shape fit was extrapolated to 1–6 nm diameter space assuming a peak at 5 nm. The emission peak at a smaller diameter than in the 30-m dataset accounted for the fact that the model horizontal grid spacing was 15 m, but the closest measurement from the freeway was at 30 m. The "No co or c/e" size distribution in Figure 2a shows the approximate shape of the total particle emission size distribution assumed here.

The shape-fitted emission distribution was assumed to consist of the sum of the emission size distributions of BC, organics, and sulfuric acid. The shape of the BC portion of

the size distribution was estimated by assuming (a) BC was not emitted into particles < 14 nm in diameter (8 (Figure 1)), (b) BC comprised 85% of total emitted aerosol mass above 29 nm, and (c) the mass fraction of BC in particles scaled linearly between 0% at 14 nm to 85% at 29 nm. The shapes of the emitted size distributions of individual organics and sulfuric acid were assumed to be the same as each other and equal to the shape of the total distribution minus that of BC.

Vehicle emission rates used were 66.1 mg/km for $\geq C_{12}$ organic vapor, 43.7 mg/km for organic particle components, 56 mg/km for BC, and 1 mg/km for S(VI) (21, for late-model medium-duty diesel trucks). Traffic on the 405 freeway consisted of 13,000 cars, 350 light trucks, and 550 heavy duty trucks per hour (3, 4). It was assumed that the average car, light truck, and heavy-duty truck emissions were $^1/_4$, 2, and 12 times those of late-model medium-duty diesel trucks, which implies that older vehicles emitted more than did newer vehicles. Additional simulations with different traffic flows and exhausts resulted in the same conceptual findings as reported here.

Total organic gas and particle mass emission rates were fractionated among species with fractions obtained from the relative emission rates of $C_{12}-C_{29}$ alkanes (21 (Table 2)) and from ambient concentrations of $C_{30}-C_{36}$ alkanes (25 (Table 1)) scaled to the emission rate of C_{29} alkanes (21 (Table 2)). For the base case, the LVLMV surrogate was set to 1% of the total organic vapor emission rate in the gas-phase plus 1% of the total organic particle emission in the particle phase. Individual component particle mass emission rates were distributed as a function of size with the shape distributions described above.

The set of $i = 1, ..., N_B$ (where N_B is the number of discrete size bins) condensation/evaporation equations and the corresponding gas conservation equation solved in each grid cell and 1-s time step for each condensable organic and inorganic species q were

$$\frac{dc_{q,i,t}}{dt} = k_{q,i,t-h}\left(C_{q,t} - \frac{c_{q,i,t-h}}{\sum_q c_{q,i,t-h}} \exp\left(\frac{2\sigma_q m_q}{r_i R^* T \rho_q}\right)C_{q,s,i,t-h}\right)$$
$$i = 1, ..., N_B \quad (1)$$

$$\frac{dC_{q,t}}{dt} =$$
$$-\sum_{i=1}^{N_B}\left\{k_{q,i,t-h}\left[C_{q,t} - \frac{c_{q,i,t-h}}{\sum_q c_{q,i,t-h}} \exp\left(\frac{2\sigma_q m_q}{r_i R^* T \rho_q}\right)C_{q,s,i,t-h}\right]\right\}$$
$$(2)$$

respectively, where t is current time (s), $t - h$ is one step back (s), $c_{q,i,t}$ is the mole concentration of particle component q (moles cm^{-3} air), $c_{q,i,t-h}/\sum_q c_{q,i,t-h}$ is the mole fraction of gas q in a multicomponent mixture, $C_{q,t}$ is vapor mole concentration (mol cm^{-3} air), $C_{q,s,i,t-h}$ is saturation vapor mole concentration over a flat, dilute surface (mol cm^{-3} air) (taken from ref 28 for each organic as a function of carbon number and temperature), σ_q is surface tension (set to 30 g s^{-2} for all organics here, a value within ± 10 g s^{-2} of almost all low- and high-molecular weight organics reported in 29), m_q is molecular weight (g mol^{-1}), r_i is particle radius (cm), R^* is the universal gas constant (8.3145 × 10^7 g cm^2 s^{-2} mol^{-1} K^{-1}), T is absolute temperature (K), and ρ_q is component density (g cm^{-3}). In addition

$$k_{q,i,t-h} = \frac{n_{i,t-h} 4\pi r_{i,t-h} D_q}{1 + \left[\frac{1.33 + 0.71 Kn_{q,i}^{-1}}{1 + Kn_{q,i}^{-1}} + \frac{4(1 - \alpha_{q,i})}{3\alpha_{q,i}}\right]Kn_{q,i}} \quad (3)$$

is the mass transfer rate (s^{-1}) of vapor to/from the particle surface (22 (eqs 16.64, 16.56)), where $n_{i,t-h}$ is the number concentration of particles (particles cm^{-3} air), D_q is the diffusion coefficient of gas q (cm^2 s^{-1}) (22 (eq 16.17)), $Kn_{q,I} = \lambda_q/r_i$ is the dimensionless Knudsen number of condensing gas q (where λ_q is the mean free path of the gas through air, cm) (22 (eq 16.23)), and $\alpha_{q,i}$ is the mass accommodation (sticking) coefficient of the gas (set to 0.7 for all organics here, 19). The denominator in eq 3 is a correction to the diffusion coefficient for collision geometry (accounting for deviations from continuum-regime growth) and for sticking probability (30).

Equation 1 accounts for Raoult's law and the Kelvin effect. Raoult's law gives the saturation vapor pressure of a solute in solution as equal to the saturation vapor pressure of the pure solute multiplied by its mole fraction in solution (31). The term $c_{q,i,t-h}/\sum_q c_{q,i,t-h}$ multiplied by $C_{q,s,i,t-h}$ on the right side of eq 1 accounts for Raoult's law. Although many exhaust organics are not so soluble in water, they are often soluble in each other, which may explain why many small exhaust particles appear as well-mixed liquid mixtures (e.g., P. Ziemann, personal communication). In such mixtures, the use of Raoult's law is necessary to modify the saturation vapor pressure of organics.

The Raoult's law correction to organic vapor pressures did not account for the nonideality of organic-containing solutions. Although techniques are available to calculate organic activity coefficients (e.g., 32−35), data for such techniques are relatively sparse for the species of interest, and the specific species of interest are not certain. The simplification of ignoring organic activity coefficients may give rise to some error. However, the Raoult's law correction was affected by the nonideality of inorganic components [H$_2$SO$_4$(aq), HSO$_4$$^-$, SO$_4$$^{2-}$, H$^+$, NH$_4$$^+$, Na$^+$, NO$_3$$^-$, Cl$^-$, NH$_4NO_3$(s)] in the same particles, since solute activity coefficient information were available for these components. Water uptake by inorganics due to hydration was also accounted for. Inorganic hydration was a function of the relative humidity, which was predicted in the 3-D model. During the short simulation, near-surface relative humidities were near 47%, which is typical for an August afternoon in Los Angeles. The change in particle composition due to inorganic activity coefficients and hydration affected the mole fraction of organics in particles, affecting organic vapor pressures through Raoult's law. However, the fraction of organics dominated that of inorganics near the roadway, as discussed in Jacobson and Seinfeld (17).

The exponential term multiplied by $C_{q,s,i,t-h}$ on the right side of eq 1 accounts for the Kelvin effect (e.g., 36 (eq 9.86)). Equations 1 and 2 were solved as in ref 24. When particles shrank below 0.8-nm diameter, the remaining semivolatile material was assumed to evaporate.

Coagulation was solved over a single size distribution containing multiple components with a semiimplicit numerical solution (37, 24). The scheme solves coagulation over a discrete size distribution with multiple size bins, conserving single-particle volume (cm^3 particle^{-1}) and particle volume concentration (cm^3 cm^{-3} air) exactly, while giving up slight accuracy in number concentration (particles cm^{-3} air), an error that diminishes toward zero with greater size-bin resolution. The scheme is positive-definite and noniterative. Comparisons of results from the solution scheme with exact solutions are given in Jacobson et al. (37).

The semiimplicit coagulation solution is written in terms of volume concentration (v), which is related to mole concentration by $v_{q,i,t} = m_q c_{q,i,t}/\rho_q$. For a discrete size distribution, the final volume concentration of component q within particles in size bin k after one time step of coagulation is

$$v_{q,k,t} = \frac{v_{q,k,t-h} + h \sum\limits_{j=1}^{k} (\sum\limits_{i=1}^{k-1} f_{i,j,k}\beta_{i,j}v_{q,i,t}n_{j,t-h})}{1 + h \sum\limits_{j=1}^{N_B} [(1-f_{kjk})\beta_{k,j}n_{j,t-h}]} \quad (4)$$

where h is the time step (s), β is the coagulation kernel (rate coefficient, cm^3 particle^{-1} s^{-1}) between two particles in size bins i and j, and

$$f_{i,j,k} = \begin{cases} \left(\dfrac{v_{k+1} - V_{i,j}}{v_{k+1} - v_k}\right)\dfrac{v_k}{V_{i,j}} & v_k \le V_{i,j} < v_{k+1} & k < N_B \\ 1 - f_{i,j,k-1} & v_{k-1} < V_{i,j} < v_k \ k > 1 \\ 1 & V_{i,j} \ge v_k & k = N_B \\ 0 & \text{all other cases} \end{cases}$$
$$(5)$$

is the volume fraction of a coagulated pair i,j partitioned into bin k. When a particle of volume v_i coagulates with a particle of volume v_j, the resulting volume of the coagulated-pair is $V_{i,j} = v_i + v_j$. This intermediate particle has volume between those of two model size bins, k and $k+1$, and needs to be partitioned between the two bins. Equation 5 gives the volume fraction of $V_{i,j}$ partitioned to bin k.

The coagulation kernel used here accounted for Brownian motion, convective Brownian diffusion enhancement, gravitational collection, turbulent inertial motion, turbulent shear, van der Waals/viscous forces, and fractal geometry. The complete set of equations describing these processes is given in Jacobson (22 (Section 15.6), please also see 17). Of the first five kernels, Brownian motion caused 97.3% of particle number loss in one set of simulations (17). Thus, Brownian motion, van der Waals/viscous forces, and fractal geometry are the most important of these processes for this study.

The most relevant parameter affecting coagulation due to van der Waals/viscous forces is the Hamaker constant (A). That affecting fractal geometry is the fractal dimension (D_f). In the base case simulations here (and in 17), it was assumed that $A = 200k_BT$ and $D_f = 1.7$ for particles ≥ 27 nm (and $D_f = 3.0$ for <27 nm). $D_f = 1.7$ for agglomerates is supported by measurements of 1.63 near the 405 freeway (38) and elsewhere (38, 39) and by diesel engine measurements of 1.46−1.9 (8−10, 40). Higher fractal dimensions ($D_f = 2$−2.8) have been measured (10, 41) using mobility radius, but the use of a mobility radius is inconsistent with the numerical treatment here (17). With respect to the Hamaker constant, a value of $A = 200k_BT$ gives enhancement factors of 3.25 for 14-nm particles, 2.3 for 28-nm particles, and 1.38 for 200-nm particles (17 (Figure 3)), which compares with measurements of 6−8, 1.4−3, and 1.16, respectively, for 14-nm graphitic carbon particles (42). Since the modeled enhancement factor is half that measured at small diameters, it is conservative. Although the smallest nanoparticles are not graphite, they coagulate with larger particles containing graphite, and although most reported Hamaker constants of organics are $<A = 82.3 \times 10^{-20}$ J at 298 K (base-case here), measurements of some (e.g., benzene: 90×10^{-20} J; chlorobenzene of 76.7×10^{-20} J (43 (Table 7)) are in range.

Equation 4 is solved in the order $k = 1, ..., N_B$. No production occurs into the first bin, $k = 1$, since $k - 1 = 0$ for the first bin in the numerator of eq 4. Thus, all necessary $v_{q,i,t}$ terms are known when each $v_{q,k,t}$ is calculated.

Once eq 4 is solved, total particle volume concentration in a size bin is calculated as $v_{k,t} = \sum_q v_{q,k,t}$. The new particle number concentration in size bin k is then trivially recalculated as $n_{k,t} = v_{k,t}/v_k$, and the mole concentrations of individual components are recalculated as $c_{q,i,t} = v_{q,i,t}\rho_q/m_q$.

Particle evolution was simulated assuming an emission line source (emission of gases and particles from dozens of adjacent grid cells lined up from south to north). A baseline case and several sensitivity cases were run for several minutes until a relative steady state in the upwind and downwind modeled concentration profiles was observed.

Results

During the baseline and sensitivity simulations, modeled near-surface wind speeds averaged 1−1.8 m/s and were close to the 1−1.5 m/s wind speeds measured during the measurement study of interest in Los Angeles (3). The wind direction was westerly, as observed in the measurement study.

Figure 2a ("No co or c/e" curve) shows the near-freeway, relative steady-state particle size distribution when neither coagulation nor condensation/evaporation was treated (gas and particle transport, turbulence, deposition, and removal were treated). The curve gives the size distribution in a well-mixed 15 m × 15 m × 5 m grid cell that the freeway lies in. The shape of the distribution results from a balance between continuous emission into the cell and 3-D dilution/transport out of the cell to the larger scale.

Figure 2a also shows the evolved size distribution near the freeway when condensation/evaporation without coagulation ("C/e only") and condensation/evaporation with coagulation ("Co+ce") were treated. When coagulation was treated with condensation/evaporation, coagulation fed back to the composition of organics in particles of a given size, affecting their vapor pressures through the Raoult's Law term of eq 1. However, the overall feedback of coagulation to vapor pressures is expected to be small since coagulation is a volume- (and mass-) conserving process, so although it affects the mole fraction of individual organics in particles of a given size, it does not affect the mole fraction of organics summed over the entire size distribution.

The "C/e only" size distribution in Figure 2a reflects evaporation of semivolatile organics from the "No co or c/e" size distribution shown in the same figure. The emitted size distribution already included the effects of initial dilution to the model grid scale, cooling to ambient temperature, and condensation of the initial hot exhaust. As the emitted distribution diluted further beyond the emission grid cell, the semivolatile organics began to evaporate immediately because, during dilution, the partial pressure of these organics quickly dropped below their vapor pressures. High-molecular-weight organics did not evaporate, except at very small size where the Kelvin effect dominated, since their bulk vapor pressures were so low. Figure 2b shows that modeled organics that evaporated from <30 nm particles were primarily $<C_{24}$ and those that remained were $\ge C_{24}$. These results are extremely consistent with measured data (7). Even C_{36} organics evaporated from particles <2 nm in diameter because the high molar volume of such organics caused the Kelvin effect, which increases exponentially with decreasing size and increasing molar volume, to overwhelm the low vapor pressure at that size. Of the total particle organic hydrocarbons emitted in the model excluding the LVLMV species, 60.6% by mass were $<C_{24}$.

Evaporation of $<C_{24}$ organics occurred primarily because, as particles diluted beyond their grid cell of emission (15 m × 15 m × 5 m, and at ambient temperature), their partial pressures decreased below their saturation vapor pressures. Because the saturation vapor pressures of $\ge C_{24}$ organics were higher than those of $<C_{24}$ organics, $\ge C_{24}$ organics did not evaporate so readily despite the fact that their molar volumes and, thus, their Kelvin effects, were greater than were those of $<C_{24}$ organics. Recondensation of evaporated organics did not occur significantly downwind because dilution continuously decreased the partial pressure of such organics with increasing distance downwind.
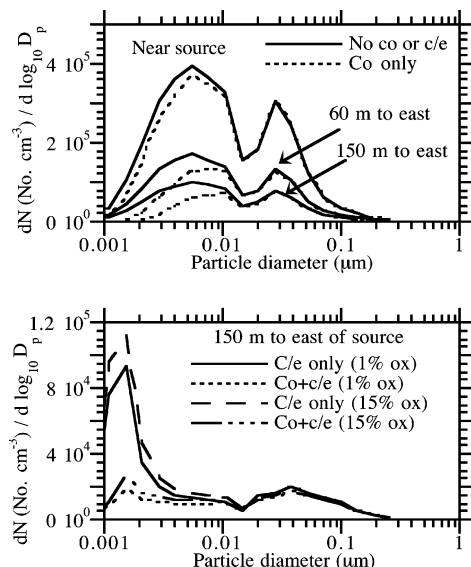
FIGURE 3. (a) Comparison of model results at the source, 60 m east of the source, and 150 m teast of the source when neither coagulation nor condensation/evaporation were treated ("No co or c/e") with those when coagulation only ("Co only") was treated (A/k_BT = 200 and D_f = 1.7 above 27 nm and = 3 below 27 nm). These results can be compared with those from Figure 2a and c. (b) Sensitivity of the result in Figure 2c to the percent LVLMV emitted. In the base case, LVLMV comprised 1% of total gas and particle emission. In the sensitivity case, it comprised 15%. The base case results are shown for reference.

The relatively small difference between the "Co+ce" and "C/e only" distributions in Figure 2a indicates that evaporation had a greater effect than did coagulation on the size distribution in the grid cell of emission. Figure 2c shows that 150 m downwind, the effect of coagulation became dominant. The figure shows the evolved size distribution 150 m (about 110 s) east of the freeway when condensation/evaporation without coagulation ("C/e only") and condensation/evaporation with coagulation ("Co+ce") were treated with different values of the Hamaker constant (A) and fractal dimension (D_f). Without coagulation ("C/e only"), modeled evaporation downwind created an unrealistically large 2–3-nm diameter concentration peak. When Brownian coagulation was treated without van der Waals forces or fractal geometry ($A = 0$, $D_f = 3$), the evaporation peak decreased partly. When van der Waals forces and fractal geometry were treated, the evaporation peak decreased more, as expected from Figure 1.

A comparison of the base case in Figure 2c ($A = 200k_BT$ and $D_f = 1.7$ for particles >27 nm) with the observed 150-m downwind distribution (Figure 4d of *3*) suggests that evaporation plus coagulation appears to explain a large portion of the observed evolution over the observed time scale (a couple of minutes between the source and downwind). Further, the number of >6 nm particles in the "Co+c/e" base case and the "C/e-only" case decreased by about 86% and 72%, respectively, from 0 to 150 m downwind, which compares with a measured decrease of 80–92% (*3* (Figure 6)), suggesting that the "Co+c/e" base case approximated the data from (*3*) better than did the "C/e only" case.

Figure 3a shows that, when coagulation was treated without evaporation, particle number concentrations decreased with increasing distance downwind, but only by 7.9%, compared with 28.3% when coagulation was treated with evaporation. Thus, evaporation enhanced the coagulation loss rate of particle number by a factor of 3.6.

Figure 3b compares 150-m results when the LVLMV surrogate comprised 15% versus 1% of organic gas+particle emission. The 15% case reduced the <5-nm mode and

increased the >20-nm mode only marginally in the absence of coagulation. Since the 15% LVLMV emission rate is much higher than measured (~0.5%, *7*) and had a small effect, condensation appears unlikely to account for the observed evolution.

Another possible explanation of the reduction in the small mode is complete evaporation of small particles. However, in the c/e-only cases in Figure 3b, no more than 25% of particles evaporated completely. When coagulation was combined with evaporation, at most 14% of particles evaporated completely.

A further explanation could be that faster diffusion of small particles enhanced their dilution relative to large particles. While true, the diffusion coefficient of even a 1-nm particle is too small to affect its dilution relative to a large particle over the spatial and temporal scale considered. This was found analytically and with the 3-D model.

Discussion

To test the relative effects of coagulation versus condensation/evaporation further, particle size distribution measurements were taken with an engine exhaust particle sizer (EEPS) instrument (*44*) at different distances along Kalder Road perpendicular to and downwind of Interstate 94 in Minnesota on October 6, 2004. The traffic flow rate was approximately 15–45 vehicles per minute and the temperature was 26 °C.

Some uncertainties in the measurements included instrument calibration uncertainty and unsteadiness in the roadway source. The instruments were not calibrated for this test sequence but relative instrument performance was evaluated on the day of the field experiment. The responses of three instruments, the EEPS, a long-column SMPS, and a 3025 condensation particle counter (CPC), to polydisperse dioctylsebacate (DOS) aerosol particles with nominal mean diameters of 50 nm gave agreement of better than 20% on total integrated number. The integrated number response of the EEPS and the 3025 CPC to sub-10-nm nucleation mode diesel aerosols gave agreement of better than 10%. The unsteadiness of the source was assessed by comparing four consecutive measurements of total number as a function of distance from the roadway. Each traverse moved from 310 to 30 m from the roadway centerline and required approximately 8 min. The 4 traverses fitted an exponential decay function of $N = 20\,000 + 98\,000\exp(-D/92)$, where N is number concentration (particles cm^{-3}) and D (m) is distance from the roadway centerline, with an average root-mean-square error of 16%. Departures from the trendline were small compared with the clear pattern of decay with distance. Figure 4a shows the composite-average EEPS-measured size distribution at different distances from the freeway, used for comparison in this study.

Three-dimensional model simulations with the same grid dimensions and spacing as in the Los Angeles case were run in an effort to simulate the measurements. The shapes of the emission size distributions for BC, organics, and sulfuric acid particle components were assumed to be the same as in the Los Angeles case. The fractionation of organics was assumed to be the same as well. The total particle mass emission rate, though, differed proportionally to the difference in the traffic flow rate. The LVLMV surrogate comprised 1% of organic gas and particle emission. Modeled winds were west to east.

Figure 4b and c show the modeled particle size distribution at nearly the same distances from the freeway along Kalder Road as in the measurements, when both coagulation and condensation/evaporation were accounted for (Figure 4b) and when coagulation but no condensation/evaporation was accounted for (Figure 4c). A comparison of Figure 4b and c with a indicates that the measured particle evolution downwind was modeled significantly better when coagulation
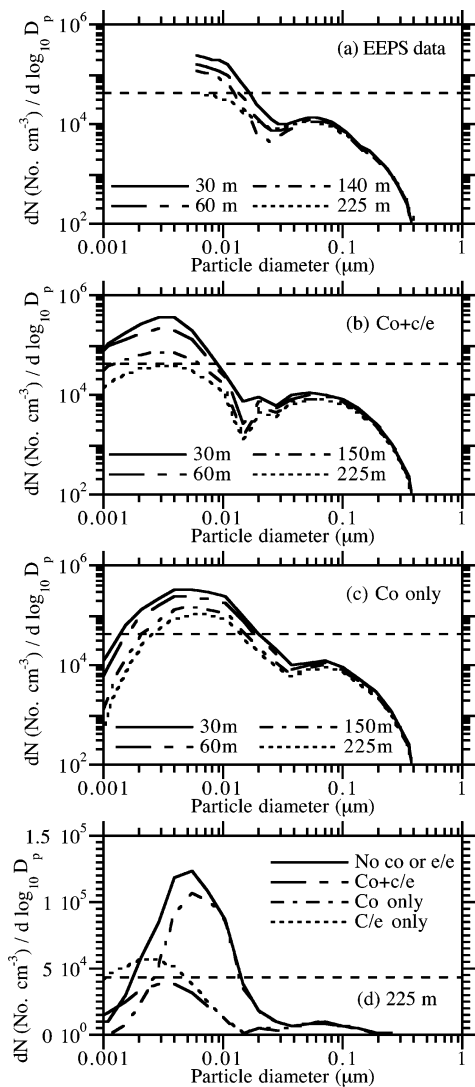
FIGURE 4. (a) Composite-average particle size distributions from several measurements by an EEPS instrument along Calder road at different distances downwind from Interstate 94, Minnesota. (b) Three-dimensional modeled size distributions at different distances from the highway when coagulation and condensation/evaporation ("Co+c/e") were treated. (c) Same as (b) but when coagulation but no condensation/evaporation was treated ("Co only"). (d) Comparison of modeled size distributions 225 m from the interstate when no coagulation or condensation/evaporation was treated ("No co or c/e"), both coagulation and condensation were treated ("Co+c/e), coagulation only was treated ("Co only"), and condensation/ evaporation only ("C/e only") was treated. The horizontal line in all figures denotes the peak of the measured size distribution at 6.04 nm diameter, 225 downwind, for reference.

was combined with evaporation than when coagulation alone was treated.

Figure 4d compares the modeled size distributions 225 m downwind when either no coagulation or condensation/evaporation was treated, both coagulation and condensation were treated, coagulation only was treated, and condensation/evaporation only were treated. The figure indicates that dilution (no coagulation or condensation/evaporation) and coagulation alone could not account for the observed peak (straight dashed line). Condensation/evaporation alone (almost exclusively evaporation) resulted in a reasonable result above 5 nm, but certainly an overestimate below 5 nm since coagulation occurs for those sizes. On the basis of this result, condensation/evaporation alone did not appear to explain the particle evolution and (b) condensation (or

recondensation of evaporated organics) following initial dilution of the hot exhaust appeared to play little role in particle evolution relative to evaporation. If condensation were important, it would have shifted the size distribution significantly to the right, worsening the comparison with data.

An additional factor yet to be considered is that puffs of emitted particles may remain isolated temporarily downwind, enhancing coagulation within them. Very fast response instruments such as the EEPS (response time <1 s) are needed to detect such microstructure in a roadway plume. To test this, the ratio of the RMS to linear time-averaged total measured number concentration was calculated. The ratio decreased from 1.3 to 1.4 near the interstate to unity about 225 m downwind, suggesting that isolated puffs existed and gradually merged downwind. Whereas, the resulting coagulation enhancement alone appeared too small to explain the rapid loss of the small mode downwind, the result suggests microstructure may play a role in particle evolution. An even faster-response instrument, not yet available, may show a greater enhancement.

In sum, this paper draws two major conclusions: (1) evaporation enhances the rate of coagulation, and (2) this factor may have an important effect on the near-source evolution of the particle size distribution under several conditions. The first conclusion appears certain based on Figure 1 and the physical laws governing the rate of coagulation due to Brownian motion. The second conclusion is less certain but appears to be supported in this study based on a comparison of model results with two independent sets of field measurements. The second conclusion depends on temperature, which affects vapor pressures and, thus, rates of evaporation. In cold air (e.g., at night), the effect is expected to be weaker than during the day. The effect also depends on particle concentration, since the coagulation rate is proportional to the product of two number concentrations. This study also finds that neither coagulation alone, condensation/evaporation alone, complete evaporation, nor preferential small-particle diffusion appear to account for observed particle evolution, as determined by comparing model results with data from two independent datasets. By contrast, the shedding of $<C_{24}$ organics from small particles appears to result in an order-of-magnitude increase in Brownian coagulation, and this increase is enhanced further by van der Waals forces and collision with larger fractals.

Major uncertainties in this study are the specific chemicals and their physical properties in exhaust nanoparticles, the emission rates of the chemicals as a function of size, and the extent to which subgrid puffs of pollutants enhance coagulation rates over rates calculated at the grid scale. On the basis of data gathered here, enhanced coagulation in isolated puffs may affect evolution. To verify further the extent to which enhanced coagulation due to evaporation may affect particle evolution, more resolved measurements of organic particle composition and particle size distributions between a roadway and 30 m downwind would be useful, since it is expected that many changes occur close to the road. In additional, a higher-resolution numerical study to examine the effect of emission puffs would be useful.

Acknowledgments

Literature Cited

(1) Hitchins, J.; Morawska, L.; Woff, R.; Gilbert, D. Concentrations of submicrometre particles from vehicle emissions near a major road. *Atmos. Environ.* **2000**, *34*, 51–59.

(2) Shi, J. P.; Evans, D. E.; Khan, A. A.; Harrison, R. M. Sources and concentration of nanoparticles (<10 nm diameter) in the urban atmosphere. *Atmos. Environ.* **2001**, *35*, 1193–1202.

(3) Zhu, Y.; Hinds, W. C.; Kim, S.; Sioutas, C. Concentration and size distribution of ultrafine particles near a major highway. *J. Air Waste Manage. Assoc.* **2002**, *52*, 1032–1042.

(4) Zhu, Y.; Hinds, W. C.; Kim, S.; Shen, S.; Sioutas, C. Study of ultrafine particles near a major highway with heavy-duty diesel traffic. *Atmos. Environ.* **2002**, *36*, 4323–4335.

(5) Kittelson, D. B. Engine and nanoparticles: a review. *J. Aerosol Sci.* **1998**, *29*, 575–588.

(6) Tobias, H. J.; Beving, D. E.; Ziemann, P. J.; Sakurai, H.; Zuk, M.; McMurry, P. H.; Zarling, D.; Waytulonis, R.; Kittelson, D. B. Chemical analysis of diesel engine nanoparticles using a nano-DMA/thermal desorption particle beam mass spectrometer. *Environ. Sci. Technol.* **2001**, *35*, 2233–2244.

(7) Sakurai, H.; Tobias, H. J.; Park, K.; Zarling, D.; Docherty, K.; Kittelson, D. B.; McMurry, P. H.; Ziemann, P. J. On-line measurements of diesel nanoparticle composition and volatility. *Atmos. Environ.* **2003**, *37*, 1199–1210.

(8) Zhu, J.; Lee, K. O.; Sekar, R. Morphological study of the particulate matter from a light-duty diesel engine. In *Proceedings of the 3rd Joint Meeting of the U. S. Sections of the Combustion Institute*; The Combustion Institute: Pittsburgh, PA, 2003. www.trans-portation.anl.gov/engine/diesel-pm.html.

(9) Wentzel, M.; Gorzawski, H.; Naumann, K.-H.; Saathoff, H.; Weinbruch, S. *J. Aerosol Sci.* **2003**, *34*, 1347–1370.

(10) Park, K.; Kittelson, D. B.; McMurry, P. H. Structural properties of diesel exhaust particles measured by transmission electron microscopy (TEM): Relationships to particle mass and mobility. *Aerosol Sci. Technol.* **2004**, *38*, 881–889.

(11) Association of European Automobile Manufacturers (ACEA). *Programme on emissions of fine particles from passenger cars*; ACEA Report, Brussels, 1999.

(12) Kittelson, D. B.; Watts, W. F.; Johnson, J. P.; Zarling, D.; Kasper, A.; Baltensperger, U.; Burtscher, H.; Schauer, J. J.; Christenson, C.; Schiller, S. Contract Final Report; U. S. Department of Energy Cooperative Agreement DE-FC04-01Al66910; Washington, DC, 2003.

(13) Vignati, E.; Berkowicz, R.; Palmgren, F.; Lyck, E.; Hummelshoj, P. Transformations of size distributions of emitted particles in streets. *Sci. Total Environ.* **1999**, *235*, 37–49.

(14) Kim, D.; Gautam, M.; Gera, D. Parametric studies of the formation of diesel particulate matter via nucleation and coagulation modes. *J. Aerosol Sci.* **2002**, *33*, 1609–1621.

(15) Wehner, B.; Philippin, S.; Wiedensohler, A.; Scheer, V.; Vogt, R. Volatility of aerosol particles next to a highway. *J. Aerosol Sci.* **2001**, *32*, S117–S118.

(16) Pohjola, M.; Pirjola, L.; Kukkonen, J.; Kulmala, M. Modelling of the influence of aerosol processes for the dispersion of vehicular exhaust plumes in street environment. *Atmos. Environ.* **2003**, *37*, 339–351.

(17) Jacobson, M. Z.; Seinfeld, J. H. Evolution of nanoparticle size and mixing state near the point of emission. *Atmos. Environ.* **2004**, *38*, 1839–1850.

(18) Gidhagen, L.; Johansson, C.; Langner, J.; Olivares, G. Simulation of NO$_x$ and ultrafine particles in a street canyon in Stockholm, Sweden. *Atmos. Environ.* **2004**, *38*, 2029–2040.

(19) Zhang, K. M.; Wexler, A. S.; Zhu, Y. F.; Hinds, W. C.; Sioutas, C. Evolution of particle number distribution near roadways. Part II: The "road-to-ambient" process. *Atmos. Environ.* **2004**, *38*, 6655–6665.

(20) Ayala, A.; Olson, B.; Cantrell, B.; Drayton, M.; Barsic, N. *Estimation of Diffusion Losses when Sampling Diesel Aerosol: A Quality Assurance Measure*; SAE Technical Paper Series 2003-01-1896; Society of Automotive Engineers: Warrendale, PA, 2003.

(21) Schauer, J. J.; Kleeman, M. J.; Cass, G. R.; Simoneit, B. R. Measurement of emissions from air pollution sources. 2. C1 through C30 organic compounds from medium duty diesel trucks. *Environ. Sci. Technol.* **1999**, *33*, 1578–1587.

(22) Jacobson, M. Z. *Fundamentals of Atmospheric Modeling*, 2nd ed.; Cambridge University Press: New York, 2005.

(23) Jacobson, M. Z. GATOR-GCMM: A global through urban scale air pollution and weather forecast model. 1. Model design and treatment of subgrid soil, vegetation, roads, rooftops, water, sea ice, and snow. *J. Geophys. Res.* **2001**, *106*, 5385–5402.

(24) Jacobson, M. Z. Analysis of aerosol interactions with numerical techniques for solving coagulation, nucleation, condensation, dissolution, and reversible chemistry among multiple size distributions. *J. Geophys. Res.* **2002**, *107*, D19 4366. doi: 10.1029/2001JD002044.

(25) Fraser, M. P.; Cass, G. R.; Simoneit, B. R.; Rasmussen, R. A. Air quality model evaluation data for organics. 4. C2–C36 non-aromatic hydrocarbons. *Environ. Sci. Technol.* **1997**, *31*, 2356–2367.

(26) Makar, P. A. The estimation of organic gas vapour pressure. *Atmos. Environ.* **2001**, *35*, 961–974.

(27) Shi, J. P.; Harrison, R. M.; Evans, D. E.; Alam, A.; Barnes, C.; Carter, G. A method for measuring particle number emissions from vehicles driving on the road. *Environ. Technol.* **2002**, *23*, 1–14.

(28) Kadowaki, S. Characterization of carbonaceous aersools in the Nagoya urban area. 2. Behavior and origin of particulate *n*-alkanes. *Environ. Sci. Technol.* **1994**, *28*, 129–135.

(29) Lide, D. R., Ed.-in-Chief. *CRC Handbook of Chemistry and Physics*; CRC Press: Boca Raton, FL, 2003.

(30) Fuchs, N. A.; Sutugin, A. G. Highly dispersed aerosols. In *Topics in Current Aerosol Research*; Hidy, G. M., Brock, J. R., Eds.; Pergamon Press: New York, 1971; Vol. 2, pp 1–60.

(31) Raoult, F.-M. General law of the vapor pressure of solvents. *Comptes Rendus* **1887**, *104*, 1430–3.

(32) Gmehling, J.; Rasmussen, P.; Fredenslund, A. Vapor-liquid equilibria by UNIFAC group contribution, revision and extension. 2. *Ind. Eng. Chem. Process Des. Dev.* **1982**, *21*, 118–127.

(33) Hansen, C. M.; Anderson, B. H. The affinities of organic solvents in biological systems. *Am. Ind. Hyg. Assoc. J.* **1988**, *49*, 301–308.

(34) Bowman, F. M.; Melton, J. A. Effect of activity coefficient models on predictions of secondary organic aerosol partitioning. *J. Aerosol Sci.* **2004**, *35*, 1415–1438.

(35) Chandramouli, B.; Jang, M.; Kamens, R. M. Gas-particle partitioning of semi-volatile organics on organic aerosols using a predictive activity coefficient model: analysis of the effects of parameter choices on model performance. *Atmos. Environ.* **2003**, *37*, 853–864.

(36) Seinfeld, J. H.; Pandis, S. N. *Atmospheric Chemistry and Physics*; Wiley-Interscience: New York, 1998.

(37) Jacobson, M. Z.; Turco, R. P.; Jensen, E. J.; Toon, O. B. Modeling coagulation among particles of different composition and size. *Atmos. Environ.* **1994**, *28A*, 1327–1338.

(38) Xiong, C.; Friedlander, S. K. Morphological properties of atmospheric aerosol aggregates. *Proc. Natl. Acad. Sci.* **2001**, *9*, 11851–11856.

(39) Katrinak, K. A.; Rez, P.; Perkes, P. R.; Buseck, P. R. Fractal geometry of carbonaceous aggregates from an urban aerosol. *Environ. Sci. Technol.* **1993**, *27*, 539–547.

(40) Lee, K. O.; Cole, R.; Sekar, R.; Choi, M. Y.; Zhu, J.; Kang, J.; Bae, C. *Detailed Characterization of Morphology and Dimensions of Diesel Particulates via Thermophoretic Sampling*; SAE 2001-01-3572; Society of Automotive Engineers: Warrendale, PA, 2001.

(41) Virtanen, A. K. K.; Ristimaki, J. M.; Vaaraslahti, K. M.; Keskinen, J. Effect of engine load on diesel soot particles. *Environ. Sci. Technol.* **2004**, *38*, 2551–2556.

(42) Burtscher, H.; Schmidt-Ott, A. Enormous enhancement of van der Waals forces between small silver particles. *Phys. Rev. Lett.* **1982**, *48*, 1734–1737.

(43) Visser, J. On Hamaker constants: A comparison between Hamaker constants and Lifshitz-van der Waals constants. *Adv. Colloid Interface Sci.* **1972**, *3*, 331–363.

(44) Johnson, T.; Caldow, R.; Pocher, A.; Minne, A.; Kittelson, D. *A New Electrical Mobility Particle Sizer Spectrometer for Engine Exhaust Particle Measurements*; SAE Technical Paper Series 2004-01-1341; Society of Automotive Engineers: Warrendale, PA, 2004.